Dynamic genome-scale modeling of *Saccharomyces cerevisiae* unravels mechanisms for ester formation during alcoholic fermentation

William T. Scott, Jr.[1,2,3]*, David Henriques[4]*, Eddy J. Smid[3], Richard A. Notebaart[3], and Eva Balsa-Canto[4]

[1]UNLOCK, Wageningen University & Research, Wageningen, The Netherlands

[2]Laboratory of Systems and Synthetic Biology, Wageningen University & Research, Wageningen, The Netherlands

[3]Food Microbiology, Wageningen University & Research, Wageningen, The Netherlands

[4] Biosystems and Bioprocess Engineering Group, IIM-CSIC, Vigo, Spain

*Address correspondence to william.scott@wur.nl and davidh@iim.csic.es

Postal Address:
Wageningen University & Research
Laboratory of Systems and Synthetic Biology
Stippeneng 4
Building 124 (Helix)
6708 WE Wageningen

ORCID: William T. Scott, Jr. - https://orcid.org/0000-0002-4029-2998, David Henriques - https://orcid.org/0000-0002-9477-292X, Eddy J. Smid - https://orcid.org/0000-0002-6687-5083, Richard A. Notebaart - https://orcid.org/0000-0003-3469-1893, and Eva Balsa-Canto - https://orcid.org/0000-0002-1978-2626

Running Title: dFBA modeling of ester formation during fermentation

SUMMARY

Fermentation employing *Saccharomyces cerevisiae* has produced alcoholic beverages and bread for millennia. More recently, *S. cerevisiae* has been used to manufacture specific metabolites for the food, pharmaceutical, and cosmetic industries. Among the most important of these metabolites are compounds associated with desirable aromas and flavors, including higher alcohols and esters. Although the physiology of yeast has been well-studied, its metabolic modulation leading to aroma production in relevant industrial scenarios such as winemaking is still unclear. Here we ask what are the underlying metabolic mechanisms that explain the conserved and varying behavior of different yeasts regarding aroma formation under enological conditions? We employed dynamic flux balance analysis (dFBA) to answer this key question using the latest genome-scale metabolic model (GEM) of *S. cerevisiae*. The model revealed several conserved mechanisms among wine yeasts, e.g., acetate ester formation is dependent on intracellular metabolic acetyl-CoA/CoA levels, and the formation of ethyl esters facilitates the removal of toxic fatty acids from cells using CoA. Species-specific mechanisms were also found, such as a preference for the shikimate pathway leading to more 2-phenylethanol production in the Opale strain as well as strain behavior varying notably during the carbohydrate accumulation phase and carbohydrate accumulation inducing redox restrictions during a later cell growth phase for strain Uvaferm. In conclusion, our new metabolic model of yeast under enological conditions revealed key metabolic mechanisms in wine yeasts, which will aid future research strategies to optimize their behavior in industrial settings.

KEYWORDS: Dynamic flux balance analysis (dFBA), Metabolic modeling, Wine, Fermentation, Yeast, Systems biology, Esters

1 INTRODUCTION

The genetics and metabolism of the yeast, *Saccharomyces cerevisiae*, have been studied extensively as a model eukaryotic organism (Botstein et al., 1997, Liti, 2015). However, despite its general use for industrial processes such as winemaking, variability in fermentation performance, especially in growth and aroma production, is not entirely understood (Hirst and Richter, 2016). Since prominent aromas, e.g., higher alcohols and esters, are partially produced during active growth, factors that affect yeast growth simultaneously influence essential aroma formation (Dekoninck, 2012). Furthermore, commercial yeast strains vary by orders of magnitude in their aroma production (Steensels et al., 2014, Gonzalez and Morales, 2017, Pérez et al., 2021). This variation has been associated with a myriad of genetic (Peter et al., 2018) and environmental factors such as nitrogen and micronutrients concentration levels (Su et al., 2021), temperature (Rollero et al., 2015), pH (Lam et al., 2014), ethanol concentration levels (Snoek et al., 2016), and the presence of toxins (Viegas et al., 1989).

Commercial strains of wine yeast respond to these factors differently in poorly understood ways, but their responses appear to be correlated with specific parts of yeast metabolism, such as those involved in lipid formation and membrane composition (Henderson et al., 2013). Moreover, it has been suggested that particular aromas are synthesized because of the detoxification of medium-chain fatty acids. It is also speculated that aroma formation is part of a metabolic process used to balance the acetyl-CoA/CoA ratio (Mason and Dufour, 2000). Understanding the differences in metabolism in yeast strains will lead to a greater ability to control and manipulate aroma-related performance. That greater metabolic understanding will facilitate insight into the specific mechanisms inducing aroma formation.

Several studies have examined the production of volatile organic compounds (VOC) or aroma (Miller et al., 2007, Carrau et al., 2008, Seguinot et al., 2018). Some of these studies have combined

omics approaches, exploring the link between yeast gene expression and metabolomics (Dunn et al., 2005, Minebois et al., 2020) or analyzing the transcriptome and metabolome profiles of yeast strains to assess the expressed genes on aroma formation during wine fermentation (Rossouw et al., 2008). Although there is experimental evidence for differences in the metabolism of various strains and genes involved in aroma formation, these experimentally-derived large data sets can be challenging to generate and analyze, especially in terms of finding the most important differences relevant to the metabolism being studied. As an alternative, mathematical modeling of yeast metabolism can provide a more comprehensive means to examine how yeast metabolism changes during the entire course of wine fermentation and which parts of overall metabolism are interrelated.

Metabolic modeling of yeast under enological conditions has been reported for some time (Boulton, 1980, Cramer et al., 2002, Sainz et al., 2003, Pizarro et al., 2007). The general approach has been to use Flux Balance Analysis (FBA) with a subset of metabolites and metabolic reactions found in yeast during alcoholic fermentation (Quiros et al., 2013), often augmented with dynamic FBA (dFBA) to account for the time-dependent nature of wine fermentations and their associated yeast metabolism. More recently, the number of metabolites and reactions included in models of *Saccharomyces cerevisiae* has grown to be more comprehensive to the point where they are often referred to as genome-scale metabolic models (GEMs).

Consensus GEMs for yeast have developed from model *iFF708* (1172 reactions) (Forster et al., 2003) to increasingly comprehensive models (Nookaew et al., 2008, Aung et al., 2013) (1413 and 3498 reactions, respectively), with the newest consensus model being *Yeast8* (3498 reactions) (Lu et al., 2019). This recent model has been further curated to include some lipid synthesis pathways and amino acid degradation pathways to account for the production of higher alcohols,

101 carboxylic, acids and esters (Scott et al., 2020), which have been proven to be key in imparting
102 desirable aromas to alcoholic beverages (for more details, see review by (Dzialo et al., 2017)).
103 Vargas et al. (2011) proposed the application of dFBA to less extensive GEMs for studying
104 wine fermentations (Vargas et al., 2011); however, that study lacked exploration into intracellular
105 flux behavior and insight into how kinetic constraints impact prediction performance. Jouhten and
106 coworkers used dFBA with *Yeast5* (Herrgård et al., 2008) to simulate the dynamic metabolic
107 response of *S. cerevisiae* exposed to sudden oxygen depletion (Jouhten et al., 2012). Also, Sanchez
108 and coworkers devised a dFBA framework with *Yeast5* to successfully calibrate different types of
109 data from aerobic fed-batch and anaerobic batch cultivations (Sánchez et al., 2014). These two
110 studies nevertheless pertained to *S. cerevisiae* grown under glucose-limited conditions while
111 nitrogen-limited growth of *S. cerevisiae* is relevant to enological conditions.
112 Yeast8 has been combined with constraint-based modeling approaches to understand yeast
113 metabolism in a few studies. However, the use of this yeast GEM has thus far been confined to
114 glucose-limited, aerobic conditions (Moreno-Paz et al., 2022), nutrient-rich cases (Henriques et
115 al., 2021b) and/or under non-transient model scenarios (Scott et al., 2021b), thus limiting its scope
116 and applicability to accurately predict enological conditions.
117 In this study, the *Yeast8.5.0* GEM (Lu et al., 2019), along with the dFBA framework proposed
118 by (Henriques et al., 2021b), were employed to predict the metabolic behavior of *Saccharomyces*
119 *cerevisiae* commercial strains under enological conditions. The dFBA framework proposed by
120 Henriques et al. has advantages versus previous dFBA frameworks using yeast GEMs because it
121 contains a multiphase multiobjective implementation of a parsimonious flux balance analysis
122 (pFBA) and a method for capturing changes in the biomass equation at different growth phases.
123 Our model framework was mainly used to model nitrogen-limited, anaerobic growth of *S.*

124 *cerevisiae* with appropriate kinetic constraints and utilizing a biomass equation tailored for
125 enological conditions. After calibrating the model with published experimental data from four
126 commercial yeast strains (Scott et al., 2021a), the goodness of fit of the model was assessed for
127 each strain to evaluate the accuracy and quality of the model simulations. We analyzed the
128 metabolic flux distributions corresponding to the best fit to the experimental data. Our analysis
129 revealed conserved behavior across strains. However, some strain-specific mechanisms were also
130 noticed, particularly in the Uvaferm and Opale strains.
131

132 **2 EXPERIMENTAL PROCEDURES**

133 **2.1 Experimental data**

134 The experimental data for this study come from a previously described study published by
135 Scott and coworkers (Scott et al., 2021a). The yeast strains used in experiments were Uvaferm
136 43™(Uvaferm), Lalvin R2™ (R2), Lalvin ICV Opale™ (Opale), and Vitilevure™ Elixir Yseo
137 (Elixir), which are all commercial strains developed by Lallemand (Lallemand, Montreal,
138 Quebec). All yeast strains were acquired from the UC Davis Enology Culture Collection.
139 Fermentations were carried out for each strain in MMM synthetic grape juice medium under
140 nitrogen-limited conditions (yeast assimilable nitrogen, YAN ~ 120 mg/L). More specifically,
141 sugar (220 g/liter; ~ 22.0oBrix), as a 1:1 mixture of glucose (110 g/liter) and fructose (110 g/liter),
142 MMM synthetic grape juice medium was prepared according to the method of Giudici and Kunkee
143 (1994), as previously reported (Henderson et al. 2011). Regarding YAN, to make one liter of
144 MMM medium, 0.1g, of ammonium phosphate, 0.1g L-tryptophan, 0.2g L-arginine*HCl, 1.0g L-
145 proline, and 2 g of vitamin-free Casamino acid were added. From analysis reported in Nolan
146 (1971), 2g of Vitamin- Casamino acid (Difco) consists of 0.649 mM, lysine, 0.194 mM histidine,

147 0.709 mM ammonia, 0.227 mM arginine, 0.029 mM cysteic acid, 0.657 mM asprartic acid, 0.417
148 mM threonine, 0.623 mM serine, 1.604 mM glutamic acid, 1.237 mM proline, 0.311 mM, glycine,
149 0.440 mM alanine, 0.600 mM valine, 0.225 mM methionine, 0.392 mM isoleucine, 0.877 mM
150 leucine, 0.007 mM tyrosine, and 0.091 mM phenylalanine (Nolan 1971). The medium also
151 contained 1000 mg/L of proline which is not commonly used by *Saccharomyces cerevisiae* as a
152 source of YAN under enological conditions. The pH of the MMM medium was adjusted to ~ 3.25
153 using 3 N KOH. All the experiments were carried out at a constant temperature of 20 °C. These
154 yeast strains were selected based on their different fermentation and aroma-producing performance
155 attributes. Furthermore, the manufacturers present qualitative characterizations of these strains,
156 but publish information that lacks quantitative distinctions (see Table 1). For additional
157 information pertaining to the media preparation, yeast strains, culture conditions, or fermentation
158 sampling that were performed to generate the experimental data used in this study, see report from
159 Scott and coworkers (Scott et al., 2021a).
160
161 Table 1. Main enological properties of select yeast strains

Commercial Name	Species	Producer	Wine Attributes
Uvaferm 43™	*Saccharomyces cerevisiae var. bayanus*	Lallemand	Restarts stuck fermentations, neutral sensory impact, low volatile acid production
Lalvin R2™	*Saccharomyces cerevisiae var. bayanus*	Lallemand	Improves secondary aroma which leads to generating fruity and floral aroma precursors and fermentation esters.

Lalvin ICV Opale™	*Saccharomyces cerevisiae var. cerevisiae*	Lallemand	Develops more volatile aromatic compounds, resulting in intense and complex fruit aromas
Vitilevure™ Elixir Yseo	*Saccharomyces cerevisiae var. cerevisiae*	Lallemand	Spurs a vigorous production of fruity and floral aromas from esters

2.2 Genome-scale metabolic model (GEM)

The GEM used in this study was *Yeast8.5.0* (Lu et al., 2019), publicly available on GitHub (see link: https://github.com/SysBioChalmers/yeast-GEM). The GEM contains 2742 metabolites, 4058 reactions, and 1150 genes. The GEM was initially developed for *S. cerevisiae* S288C, a haploid laboratory strain that is not employed in winemaking. However, since this study was applied to fermentations under enological conditions, we modified the GEM to appropriately reflect the anaerobic state of metabolism. In our approach, we proceeded as suggested by Heavner and coworkers (Heavner et al., 2013), constraining v_{O_2} to zero (LB=UB=0 [mmol/g DW h]), allowing unrestricted uptake of ergosterol (r_1757), lanosterol (r_1915), zymosterol (r_2106), 14-demethyllanosterol (r_2134), and ergosta-5,7,22,24(28)-tetraen-3beta-ol (r_2137) and oleate (r_2189). In addition, pathways including the oxaloacetate-malate shuttle and glycerol dehydrogenase reaction were unrestricted as described by Sanchez and coworkers (Sánchez et al., 2017, Sánchez et al., 2019) (in the model, this was achieved by blocking reactions r_0713, r_0714, and r_0487). Heme A was also removed since it is not used under anaerobic conditions. All the changes related to anaerobiosis were applied either at the beginning of the fermentation or after the depletion of the initially dissolved oxygen in the simulated media. Moreover, *Yeast8.5.0* includes expanded coverage of aroma-associated pathways such as an extended Ehrlich pathway,

180 more ester formation reactions, and enhanced sulfur reduction pathways as previously performed
181 and described in the literature (Scott et al., 2020).

182 The GEM used in this study differs from that used in the (Henriques et al., 2021b) study.
183 Henriques et al. expanded *Yeast8* (*v.8.3.*1) to include 38 metabolites and 50 reactions to explain
184 secondary metabolism. Furthermore, 13 aroma-impact molecules were added to GEM (see Table
185 S1 in (Henriques et al., 2021b) for more details). The GEM used in this work is *Yeast8* (*v.8.5.0*).
186 This version of *Yeast8* contains at least 72 reactions and 50 metabolites related to amino acid
187 degradation and ester synthesis, which induce the formation of some aroma compounds. Moreover,
188 *Yeast 8.5.0* expanded coverage is based on the work of (Scott et al., 2020) (see version release
189 details for the complete list of updates here: https://github.com/SysBioChalmers/yeast-
190 GEM/releases).

191 **2.3 Flux balance analysis**

192 Flux balance analysis (FBA) (Varma and Palsson, 1994, Orth et al., 2010) is a modeling
193 framework based on knowledge of reaction stoichiometry and mass/charge balances. The
194 framework relies on the pseudo-steady-state assumption (no intracellular accumulation of
195 metabolites occurs). The well-known expression captures FBA:

196 $$\mathbf{S} \cdot \mathbf{v} = \mathbf{0}$$

197 where **S** is the stoichiometric matrix of (*n* metabolites by *m* reactions), and **b** is a vector of
198 metabolic fluxes. The number of unknown fluxes is higher than the number of equations; thus, the
199 system is undetermined. Still, it is possible to find a unique solution under the assumption that cell
200 metabolism evolves to pursue a predetermined goal which is defined as the maximization (or
201 minimization) of a particular objective function (J):

202

$$\max J$$

$$s.t.: \quad \mathbf{S} \cdot \mathbf{v} = \mathbf{0}$$

$$\mathbf{LB} < \mathbf{v} < \mathbf{UB}$$

where **LB** and **UB** correspond to the lower and upper bounds on the estimated fluxes. Examples of objective functions J include growth rate, ATP, or the negative of nutrient consumption, etc.

The solution to an FBA problem is often not unique, i.e., several different combinations of fluxes may lead to the same optimum. A common approach to finding a single solution is to further constrain the problem with prior knowledge or biological intuitions. Often, the so-called parsimonious FBA (pFBA) is used. The underlying idea is to find the solution that minimizes overall flux through the metabolic network (a proxy for minimizing the total necessary enzyme mass to implement the optimal solution). (Lewis et al., 2010, Machado et al., 2014).

2.4 Parameter estimation.

Parameter estimation aims to compute the unknown parameters - growth-related constants and kinetic parameters - that minimize some measure of the distance between the data and the model predictions. The maximum-likelihood principle yields an appropriate measure of such a distance (Walter and Pronzato, 1997):

$$J_{mc}(\theta) = \sum_{k=1}^{n_{exp}} \sum_{j=1}^{n_{obs}} \sum_{i=1}^{n_{st}} \left(\frac{y_{k,j,i}(\theta) - y_{k,j,i}^{m}}{\sigma_{k,j,i}} \right)^2 ,$$

where n_{exp}, n_{obs} and n_{st} $\sigma_{k,j,i}$, $y_{k,j,i}^{m}$, $y_{k,j,i}^{m}$ and $C^{m}y_{k,j,i}(\theta)$ corresponds to model predicted values, X and C. Observation functions were included for CFUs and OD_{600} to scale viable cell mass (X_V) and active cell mass (X_A), respectively.

Parameters are estimated by solving a nonlinear optimization problem where the aim is to find the unknown parameter values (θ) to minimize $J_{mc}(\theta)$ subject to the system dynamics - the model- and parameter bounds (Balsa-Canto et al., 2010).

To assess the confidence in the parameter estimates we estimated the covariance matrix from the Fisher Information Matrix:

$$\left| F = E_{y_{m|\theta^*|}} \left\{ \left[\frac{dJ_{mc}(\theta)}{d\theta} \right] \left[\frac{dJ_{mc}(\theta)}{d\theta} \right]^T \right\} \right|$$

where E represents expected value and θ* is the optimal parameter value. Remark that the evaluation of the derivatives of the log-likelihood function (J_{mc}) with respect to the parameters, requires the computation of the sensitivities of the measured states with respect to the parameters. The Cramèr-Rao inequality provides a lower bound on the covariance of the estimators:

$$C \geq F^{-1}(\theta^*)$$

The confidence interval for a given parameter is then given by:

$$t_{\frac{\alpha}{2}}^{\gamma\sqrt{C_{ii}}}$$

where $t^{\gamma}_{\alpha/2}$ is given by the Students t-distribution, γ regards the number of degrees of freedom and α is the (1-α) 100% confidence interval.

2.5 The Multi-Phase Multi-Objective Flux Balance Analysis Framework

In this work, we have adapted the model described in (Henriques et al., 2021b) that accounts for the dynamic nature of batch fermentation and divides the process into five phases: the lag phase, exponential growth, growth under nitrogen limitation, stationary phase, and decay. Each

240 phase is characterized by a cellular objective and a set of constraints. Their duration is imposed by
241 the estimated parameters TL, TCA, TS, and TD. Interested readers can find a detailed description
242 of the model equations for the different phases (Henriques et al., 2021b). Here we summarize some
243 of the most relevant characteristics for each phase:

244 • Lag phase: The objective is to maximize ATPase expenditure (equivalent to maximizing
245 ATP production).
246 • Exponential growth phase (until the nitrogen sources were nearly exhausted): The objective
247 is to maximize the growth rate.
248 • Carbohydrate accumulation phase: The objective is to maximize protein production with
249 constrained carbohydrate accumulation.
250 • Stationary and decay phases: The objective is to maximize ATP and protein production.

251 These objectives were chosen assuming that cells behave optimally throughout the process.
252 Typically, the cellullar objective is assumed to be maximizing biomass. However, in batch
253 conditions, it is observed that growth is not possible in specific phases. In those phases we assume
254 that cells will behave efficiently to conserve existing biomass. In particular, we chose protein and
255 ATP maximization objectives during the carbohydrate, stationary, and decay phases. The rationale
256 behind is that yeast cells are subject to protein turnover and when it is not possible to sustain
257 growth, yeast cells will try to retain as much nitrogen as possible. Further, enforcing maximum
258 ATP production, we assume that metabolism will be as energy efficient as possible.

259

260 Constraints on the external fluxes were modeled using kinetic models in ordinary differential
261 equations. The transport of hexoses was described using Michaelis-Menten-type kinetics subject

262 to non-competitive inhibition of ethanol (Hjersted et al., 2007). The production of ethanol, the
263 highest alcohols, carboxylic acids, and esters, was proportional to the amount of hexoses
264 transported. The transport of nitrogen sources was encoded with Michaelis-Menten-type kinetics
265 for the case of ammonia and mass action for the amino acids.

266 During the exponential phase, the protein content on the biomass was assumed to be 50%. The
267 level of mRNA is assumed to be proportional to the protein content. Maintenance of growth-
268 associated ATP (GAM) was also updated to account for the polymerization costs of the different
269 macromolecules (proteins, RNA, DNA, and carbohydrates):

270 $$GAM = GAM_F + GAM_{Prot} + GAM_{RNA} + GAM_{Carbs} + GAM_{DNA}$$

271 where GAM_F is a species or strain-dependent parameter estimated from the data, and the rest are
272 the polymerization costs of the different biomass precursors (adapted from (Lu et al., 2019)). All
273 scripts necessary to reproduce the results are distributed
274 (https://sites.google.com/site/amigo2toolbox/examples).

275 **2.6 Analysis of dynamic metabolic fluxes.**

276 Here, we evaluated metabolic pathways using a flux ratio, which measures net flux over time
277 during growth and stationary phases. In particular, we computed the integral of each flux
278 multiplied by the biomass (mmol . h $^{-1}$) over time and normalized its value with the accumulated
279 flux of consumed hexoses (glucose and fructose):

280

281 $$S_{i.G} = \frac{\int_{T_L}^{T_S} v_i(t).DW(t)}{\int_{T_L}^{T_S} v_{Glx}(t).DW(t) + \int_{T_L}^{T_S} v_F(t).DW(t)}$$

282 $$S_{i.CA} = \frac{\int_{T_E}^{T_S} v_i(t) \,.\, DW(t)}{\int_{T_E}^{T_S} v_{Glx}(t) \,.\, DW(t) + \int_{T_E}^{T_S} v_F(t) \,.\, DW(t)}$$

283 $$S_{i.D} = \frac{\int_{T_S}^{T_D} v_i(t) \,.\, DW(t)}{\int_{T_S}^{T_D} v_{Glx}(t) \,.\, DW(t) + \int_{T_S}^{TD} v_F(t) \,.\, DW(t)}$$

284

285 where $S_{i,G}$ corresponds to the flux score *i* during growth, $S_{i,CA}$ corresponds to the score during
286 stationary and $S_{i,D}$ decay phases, $v_i(t)$ (mmol . h^{-1} . DW^{-1}) is the flux under scrutiny, $v_{Glx(t)}$ (mmol
287 . h^{-1} . DW^{-1}) is the glucose flux, $v_{Fr(t)}$ (mmol . h^{-1} . DW^{-1}) is the flux of fructose and DW is the
288 predicted dry weight biomass (g). The results correspond to the mmol of compound produced per
289 mmol of hexose consumed x 100 (denoted mmol / mmolH). Score values indicate the overall
290 impact of each reaction in the net oxidation or reduction of electron carriers during the given phase
291 of fermentation.

292 **2.7 Computing Environment**

293 The modeling was performed in MATLAB® 2020b (The MathWorks, Inc., Cambridge, MA,
294 USA) using Cobra Toolbox 3.0 (Heirendt et al., 2019) and implemented on a Windows 10
295 (Microsoft Corporation, Redmond, WA, USA) Intel® (Intel Corporation, Santa Clara, CA, USA)
296 Core™ i7-7500 CPU @ 2.70 GHz–2.90 GHz processor. The GEM was imported into MATLAB
297 as an SBML file and curated using Cobra Toolbox. Git version 2.3.0 was installed before cloning
298 COBRA with GitHub and initializing COBRA in MATLAB.

299 The multi-phase multi-objective genome-scale model framework was implemented as a script
300 for AMIGO2 toolbox (Balsa-Canto et al., 2016) to facilitate parameter estimation, simulation, and
301 quality of fit analyses. From the possibilities available in AMIGO2, we selected to solve the model

using the initial value problem solver CVODES (Hindmarsh et al., 2005) and a Nelder-Mead method (fminsearch, in MATLAB) to optimize parameter values in reasonable computational time. In addition, the tool automatically computes the FIM-based confidence intervals for the optimal parameter values.

3 RESULTS AND DISCUSSION

3.1 Multi-phase multi-objective dynamic flux balance analysis framework

We adapted the model reported earlier (Henriques, et al., 2021) to describe the intracellular fluxes. Here, we divided the process into five phases in which cellular objectives and flux constraints must be adapted: lag, exponential growth, carbohydrate accumulation, stationary, and decay (see Fig. 1). The duration of the phases was determined by the parameters t_L, t_E, t_s, and t_D.

In its original version, the model relied on a dynamic biomass equation dependent on the amount of YAN in the medium. Nevertheless, this equation required estimating several parameters without information about biomass composition (protein, mRNA, carbohydrates). In addition, the model could not accurately explain the observed behavior of the non-*cerevisiae* species (Uvaferm). This strain showed a long growth period with virtually no nitrogen sources available. To address this, we replaced the phase regarded as growth under nitrogen limitation with a phase characterized by carbohydrate accumulation (see (Henriques et al., 2021a) for further details).

Most nitrogen sources, except glycine, were consumed primarily during the exponential growth phase. In this period, the cellular objective was the maximization of biomass. In contrast to the previous model, during carbohydrate accumulation, we assumed cells maximize protein and activated the procedure to simulate protein turnover (described in (Henriques et al., 2021b)) . Also, to simulate carbohydrate accumulation during this period, an exchange flux for this compound (s_3717[c]) was added to the stoichiometric network determined by the equation:

325 $$v_{carb} = \tau_{Carb} \cdot \left(\theta_{Carb} - \frac{X_{Carb}}{X}\right),$$

326 where X_{Carb}(g/L) is the carbohydrate quantity present in the biomass, X is the biomass (g/L), θ_{Carb}
327 is the final carbohydrate content and τ_{Carb} is the parameter controlling the convergence rate
328 towards θ_{Carb} (see supplementary code example (dynamic genome-scale modeling of yeast
329 fermentation): https://sites.google.com/site/amigo2toolbox/examples).

330 Higher alcohol production can occur due to the assimilation/catabolism of amino acids or
331 due to *de novo* synthesis. In its previous version, the model considered that higher alcohol
332 production started during growth under nitrogen limitation and was prolonged through the
333 stationary phase. The experiments considered in that work included ammonium diphosphate
334 supplementation, and the final concentrations of higher alcohols were higher than those found in
335 the present work. Here, the relative contributions of higher alcohols produced during the first hours
336 of growth were relevant. Thus, to account for this effect, during exponential growth, we set the
337 production of isoamyl alcohol, 2-phenyl ethanol, and isobutanol at the same flux as the
338 consumption of the corresponding amino acids (leucine, phenylalanine, and isoleucine).

339

340 **3.2 Goodness of fit of the model against enological fermentation data**

341 This study employed data from experimental fermentations carried out under enological
342 conditions (see (Scott et al., 2021a)) to calibrate model parameters. The final model contained 50
343 ODEs, consisting of 60 parameters determined from time-course data for all measured
344 extracellular metabolites and biomass. The best fit to the data for glucose and fructose uptake, and
345 the secretion of ethanol, acetate, malate, succinate, and glycerol, are shown in Fig. 2 for the four
346 strains. For the primary metabolites, glucose in the medium was consumed first, followed by
347 fructose since hexose transporters in the cytoplasm have a higher affinity for the former (Fig. 2).

348 A stoichiometrically accurate yield of ethanol (~101 g/L) was predicted for the strains, reaching
349 an average simulated concentration of 100 g/L with the initial starting concentration of total sugar
350 used in this study (~220 g/L) (Fig. 2). Moreover, the values were within the range of similar
351 enological fermentations (Ribéreau-Gayon et al., 2000). Various other essential extracellular
352 metabolites are also measured and predicted throughout fermentation (Fig. 2), including glycerol,
353 malate, succinate, and acetate, with average yields among strains of ~7 g/L, ~3.2 g/L, ~1.4 g/L,
354 and ~0.5 g/L, respectively.

355 Consumption of glucose and fructose, and production of ethanol simulations were
356 representative of the enological conditions achieving excellent fits against the experimental
357 dynamic profiles (with median R^2 values of 0.98, 0.96, and 0.98 among the strains) (see Fig. 2 and
358 Table S1). YAN and biomass (dry cell weight) curves were also successfully predicted for all the
359 strains, where the median R^2 values among the strains are 0.92 and 0.96, respectively (see Table
360 S1). In addition, the production of some essential by-products of wine fermentation, including
361 glycerol, succinate, and acetate, were successfully simulated by the model achieving moderately
362 good fits among the strains with median R^2 values of 0.89, 0.81, and 0.77 (Fig. 2 and Table S1).
363 Maximum glycerol (~6.9 g/L) and succinate (~1.3 g/L) produced during the fermentation were
364 quantitatively well predicted using the model, while acetate (~0.5 g/L) prediction was reasonably
365 good (Fig. 2).

366 The nitrogen consumed by the yeast was in the form of amino acids and ammonium in the
367 MMM synthetic grape medium, and the model profiles for the nitrogen sources for the four strains
368 are shown (Fig. 3). As expected, since it has been well documented that wine fermentations are
369 nitrogen-limited as suggested in several studies (Ingledew and Kunkee, 1985, Cramer et al., 2002,
370 Varela et al., 2004), the yeast assimilable nitrogen (YAN) (a measure of the concentration of all

371 nitrogen in the free amino acids and ammonium) was consumed very rapidly. At that point, the
372 maximum cell density was reached. Figures 2, 3, and 4 showed a mixture of AA and NH_3. The
373 dFBA also accurately simulated the profiles of several important VOCs for the four strains (Fig.
374 4).

375 For the consumption of nitrogenous compounds, the model simulations obtained excellent
376 fits against experimental data with each of the amino acid dynamic profiles containing a median
377 $R^2 > 0.92$ except for histidine (0.83), lysine (0.80), and asparagine (0.79). The model also
378 simulated kinetic curves that were in reasonably good agreement with experimental data for the
379 VOCs for most strains that have $R^2 > 0.85$ (see Table S1). However, the VOCs of some strains
380 (Opale and R2) e.g., ethyl hexanoate were predicted with an $R^2 = 0.22$ and 0.16, respectively (Table
381 S1 and Fig. S2). There was only a slight underprediction of propanol for the Uvaferm strain (see
382 Fig. 3).

383 When examining the dynamic concentration profiles, the most apparent differences among
384 the strains correspond to extracellular metabolites associated with core carbon, nitrogen, and lipid
385 metabolism. These notable differences are evident when observing the secretion dynamics of
386 acetate, glycerol, and succinate (Fig. 2) as well as the overall production of many VOCs, e.g.,
387 propanol, isoamylol, isobutanol, isoamyl acetate, phenylethyl acetate, and ethyl butanoate (Fig. 3
388 and Fig. 4).

389

390 **3.3 Key flux predictions across various cell phases suggest the most distinct strain behavior**
391 **occurs during the carbohydrate accumulation phase**

392 The model framework was employed to elucidate the metabolic mechanisms adopted by
393 the strains to achieve different compound concentration levels. Using the *Yeast 8.5.0* combined

394 with the dFBA model framework, it is possible to predict the change of the entire set of fluxes
395 throughout the simulated fermentation. The dynamic flux ratios were determined using the
396 aforementioned equations (see Section 2.5 in Materials and Methods). Their values for some of
397 the key intracellular fluxes between 6- and 40-hours during fermentation (carbohydrate
398 accumulation phase) are presented in Supplementary Figure S1.

399 Essential fluxes concerning an anaerobic nitrogen-limited yeast phenotype were observed
400 in all growth phases (see supplementary data files). . These fluxes pertained to specific pathways
401 of the central carbon, nitrogen, and lipid metabolism. This key set of fluxes suggests the role of
402 NAD-dependent acetaldehyde dehydrogenase (r_2115) to restoring redox balance and allow
403 anaerobic growth at differing levels among the strains as suggested previously (Vargas et al., 2011,
404 Scott et al., 2021b). The model predictions for growth were similar among the strains except for
405 the Uvaferm strain, which experienced a later onset of stationary phase (150 h) compared to other
406 strains (80 h) (Table S1). This distinction could be related to dissimilarity in protein turnover and
407 synthesis especially pertaining to the Uvaferm strain.

408 The dynamic flux ratios pointed to aspartate-semialdehyde dehydrogenase ($\tilde{s} = 6.33 \times 10^{-}$
409 ^{4}, 1.05×10^{-3}, 1.22×10^{-4}, and 9.36×10^{-4} mmol/mmolH for Opale, R2, Elixir, and Uvaferm
410 respectively), homoserine dehydrogenase ($\tilde{s} = 6.33 \times 10^{-4}$, 1.05×10^{-3}, 1.22×10^{-4}, and $9.36 \times 10^{-}$
411 ^{4} mmol/mmolH for Opale, R2, Elixir, and Uvaferm respectively) , and glycerol-3-phosphate
412 dehydrogenase ($\tilde{s} = 7.10 \times 10^{-2}$, 8.00×10^{-2}, 6.31×10^{-2}, and 7.95×10^{-2} mmol/mmolH for Opale,
413 R2, Elixir, and Uvaferm, respectively) (where mmolH is millimoles of consumed hexose) (shown
414 as r_0219, r_0547, and r_0492 in Fig. 2) as the responsible for strain-dependent behavior. These
415 differences relate to the variation in extracellular productions of glycerol and succinate (Fig. 2 a,
416 d) The homoserine dehydrogenase enzyme is involved withing the aspartate where it regulates the

417 NAD(P)-dependent reduction of aspartate beta-semialdehyde into homoserine which subsequently
418 leads the biosynthesis of methionine, threonine, and isoleucine. In addition, the glycerol-3-
419 phosphate dehydrogenase enzyme is responsible for catalyzing the NADH-aided reduction of
420 dihydroxyacetone phosphate to glycerol 3-phosphate which leads to the biosynthesis of
421 phospholipids.

422 As nitrogen limitation conditions arise, yeast metabolism circulates more sugar flux into
423 the fermentation. As such, there is a decline in cell growth, and what is not spent (sugar, nitrogen,
424 etc., flux) on biomass synthesis is directed to other routes. Overall, for Uvaferm, the decline in
425 protein synthesis and lipid production lowered the demand for NADPH (see fluxes Table S2). At
426 the onset of carbohydrate accumulation due to nitrogen limitation, restriction of NAD+ occurred.
427 As nitrogen limits the rate of glucose and fructose uptake in conjunction with growth, the model
428 opted to employ the glyoxylate cycle to reduce NADH production while still producing necessary
429 tricarboxylic acid (TCA) cycle intermediates (Fig. 2). Overall, in this regard, the model simulations
430 underscore the tight link between glycolysis, the TCA cycle, lipid, and amino acid metabolism
431 under nitrogen-limited conditions.

432 Under nitrogen-limited fermentation conditions, sluggish fermentation can occur due to
433 lower relative protein turnover, resulting in higher relative amounts of RNA and storage
434 carbohydrates, e.g., trehalose (Varela et al., 2004). Furthermore, the release of C6 sugars from
435 trehalose and glycogen mainly occurs during the onset of the stationary phase (Schulze et al.,
436 1996). For the strains in this study excluding the Uvaferm, this release was predicted to occur at
437 the carb. accumulation phase Uvaferm showed comparably lower flux values for both the
438 carbohydrate pseudo-reaction (r_4048: $\tilde{s} =$ 8.51 x 10^{-3} mmol/mmolH) and trehalose-phosphatase
439 (r_1051: $\tilde{s} =$ 1.18 x 10^{-3} mmol/mmolH). However, Uvaferm was the only strain to have predicted

440 flux for both reactions during the stationary phase. This particularity suggests intracellular
441 mechanisms bring about carbohydrate storage or accumulation for the other strains or later for
442 Uvaferm. Furthermore, a later carbohydrate accumulation could affect the fermentative
443 performance and capacity of the yeast strain (François and Parrou, 2001, Pérez-Torrado and
444 Matallana, 2015).

445 Yeast cells produced most of the succinate during the carbon accumulation phase, where
446 the Uvaferm strain contained a higher dynamic flux ratio than the other strains (Table S3, e.g.,
447 r_1000). This higher succinate concentration in Uvaferm is caused by cells taking up a preferred
448 nitrogen source, i.e., glutamate via the GABA shunt which becomes deaminated by NAD+
449 dependent glutamate dehydrogenase to discharge α-ketoglutarate and ammonium (Fig. 2, r_0471).
450 Consequently, the increase in the intracellular α- ketoglutarate concentration increases enzyme
451 activities of the oxidative branch of the TCA cycle, causing succinate production. Previous works
452 have alluded to the fact that carbon skeletons derived from deaminated glutamate are easily
453 facilitated into the TCA cycle and, hence, transformed into succinate (Tesnière et al., 2015). This
454 premise is supported by the model, which uses an aspartate transaminase-associated reaction
455 (r_0216) to link glutamate and thus steer succinate formation (Fig. 3).

456 Although Uvaferm strain experienced substantial flux ($\tilde{s} > 1x10^{-6}$ mmol/mmolH) in many
457 reactions associated with redox balance and acetyl CoA (e.g., r_2242, r_2266, r_2274, and r_2278,
458 r_2279 as shown in Fig. 4) during the stationary phase while the other strains did not show any
459 flux, the intracellular behavior differs among the strains with higher standard deviations (see
460 supplementary data) most significantly during the carbohydrate accumulation phase. The
461 exponential and carbohydrate accumulation phases also coincide with the vigorous production of
462 higher alcohols and esters, desirable in fermented beverages such as wine and beer and

463 commercially crucial for fragrances (for more info see Fig. S1 and S2). For instance, isoamyl
464 acetate known for producing fruity aromas, experienced predicted $\tilde{s} = 6.5 \times 10^{-5}$, 5.3×10^{-5}, $6.5 \times$
465 10^{-5}, and 6.8×10^{-5} mmol/mmolH during the exponential and carbohydrate acc. phases whereas
466 during the stationary phase the Uvaferm strain was the only strain to experience a flux which was
467 6.8×10^{-5} mmol/mmolH.
468

469 **3.4 The role of acetate and ethyl esters in the transitions from growth to the stationary phase**

470 Esters are a class of compounds that imbue a range of desirable fruity and floral aromas to
471 wines and beer (Hirst and Richter, 2016). These esters are produced by a condensation reaction
472 between acetyl or acyl-CoA and an alcohol (Saerens et al., 2010). Two types of esters are
473 synthesized, acetate esters and fatty acid ethyl esters, respectively, based on whether acetyl- CoA
474 or acyl-CoA is employed when forming them (Dzialo et al., 2017). More specifically, acetate esters
475 are synthesized via the condensation of higher alcohols with acetyl-CoA, catalyzed by alcohol
476 acetyltransferase enzymes (AATs) (Mason and Dufour, 2000). Acetate esters, primarily ethyl
477 acetate, isoamyl acetate, isobutyl acetate, and 2-phenylethyl acetate, are quantitatively the most
478 abundant type of esters formed during fermentation.

479 Our modeling analysis illustrated that acetate ester production was predominately
480 modulated by the shifting of the acetyl-CoA/CoA ratios as the yeast cells transitioned from the
481 exponential to the carbohydrate accumulation phase. This reflection was seen most strikingly from
482 examining reactions associated with acetyl-CoA synthetase, alcohol acetyltransferase, malate
483 synthase, and serine O-acetyltransferase (*ACS*s, *ATF*s, *MS*, and *SAT* related to reactions: r_0112,
484 r_0113, r_0158 - r_0162, r_0716, and r_0992) where the strains that maintained the highest flux
485 ratios between phases, produced the most acetate esters.

486 For instance, during the exponential phase, the model predicted a significant flux from
487 isoamylol to isoamyl acetate inside the cytoplasm ($\tilde{s}$ = 6.5 x 10^{-5}, 5.3 x 10^{-5}, 6.5 x 10^{-5}, and 6.8 x
488 10^{-5} mmol/mmolH for Opale, R2, Elixir, and Uvaferm respectively; Fig. 4.; r_0160). This reaction
489 sustained the same fluxes for all the strains during the carbohydrate accumulation phase. The same
490 behavior was also observed in other ATF-associated reactions. In this reaction (r_0160), acetyl-
491 CoA is consumed to form CoA, thereby illustrating that strains with higher flux ratios of acetyl-
492 CoA/CoA were superior in producing higher acetate ester fluxes. This simulation result has been
493 previously explored experimentally by Hong and co-workers (Hong et al., 2019). They showed
494 that acetate ester formation in yeast is modulated by changing the CoA and acetyl-CoA levels by
495 deleting and overexpressing the *BAP2* and *ATF1*genes, respectively (Hong et al., 2019).
496 Furthermore, it has been shown that commercial yeast strains differ in the production of acetate
497 esters, by orders of magnitude, even under identical fermentation conditions (Steensels et al.,
498 2014). Our model and those previous results suggest that optimizing the activity of genes
499 responsible for regulating acetyl-CoA/CoA could be beneficial in obtaining the appropriate acetate
500 ester yield. For example, a researcher could adapt a platform tuning the enzyme expression of
501 acetyl-CoA carboxylases for acetate esters, similar to a recent study for improving supplies of
502 acetyl CoA and NADPH and eventual production of 3-hydroxypropionicacid (Qin et al., 2020).
503 Although there is much certainty regarding the mechanisms that form acetate esters during
504 fermentation, the mechanisms, including genetics and regulation of fatty acid ester formation, are
505 still less clear. However, medium-chain fatty acids (MCFA) intermediates are prematurely
506 released from the cytoplasmic fatty acid synthase (FAS) complex during the late exponential
507 growth phase. This release triggers ester synthesis as pointed out by (Taylor and Kirsop, 1977).
508 Subsequently, CoA can activate an MCFA in combination with ATP and ethanol to enzymatically

509 form an MCFA-ethyl ester (Saerens et al., 2010). This mechanism can be observed in our
510 predictions in Fig. 4 (e.g., r_4631). Additionally, transitions in fluxes were noticed in FAS
511 reactions (r_2140 and r_2141, fatty-acyl-CoA synthase) from the exponential growth phase to the
512 carbohydrate accumulation phase. For instance, these shifts in flux values among the strain
513 between growth phases could correspond to the activity in CoA with MCFA. This elaborate
514 relationship causes the levels of fatty acid esters to depend significantly on lipid metabolism and
515 acetyl-CoA.

516 Several investigations indicate at least three modulating routes for the flow of MCFAs to
517 produce ethyl esters. Firstly, the upregulation of fatty acid synthases (*FAS1* and *FAS2*) and
518 acyltransferases (*EEB1* and *EHT1*) (Saerens et al., 2010). Secondly, reduced acetyl-CoA
519 carboxylase activity has been shown to play a role where the inhibition of acetyl-CoA carboxylase
520 facilitates the discharge of MCFAs from the *FAS* complex (Hirst and Richter, 2016). Thirdly, an
521 increase in MCFA concentrations induces higher concentrations of ethyl esters in wine (Saerens
522 et al., 2008).

523 Here, it was inferred the model is in line with the hypothesis that these three routes play a
524 significant factor in producing MCFA ethyl esters. Higher fluxes during the exponential and
525 carbohydrate accumulation phases in reactions associated with fatty-acyl-CoA synthase (n-
526 C16:0CoA), fatty-acyl-CoA synthase (n-C18:0CoA), alcohol acyltransferase (butyryl-CoA), and
527 alcohol acyltransferase (hexanoyl-CoA) (r_2140, r_2141, r_4631, and r_4629) resulted in the
528 higher overall production of ethyl butanoate and ethyl hexanoate – essential MCFA ethyl esters
529 found in wines - for the Uvaferm and Opale strains (Fig. 4 and 5). For instance, Uvaferm and Opale
530 experienced 71.1% and 12.6%, respectively, more flux than the Elixir strain for the reaction
531 associated with fatty-acyl-CoA synthase (n-C16:0CoA), which resulted in 14.4% and 8.2% more

532 overall production for Uvaferm and Opale, respectively, than the Elixir strain. Conversely, when
533 examining the effect of acetyl-CoA carboxylase, the strain (R2) that experienced the lowest flux
534 value for an acetyl-CoA carboxylase-associated reaction (r_0109) during the exponential phase
535 showed the highest flux for the formation of ethyl butanoate during the carbohydrate accumulation
536 phase ($\tilde{s} = 6 \times 10^{-6}$ mmol/mmolH, r_4646).

537 Lastly, a relationship was deduced by observing the intracellular fluxes related to the
538 production and consumption of CoA (Fig, 5). For instance, we could see an uptick or higher flux
539 in ethyl esters for the strains that experienced more significant imbalances of CoA and acetyl-CoA
540 (based on greater flux values in the direction of acetyl-CoA consumption). After evaluating the
541 difference in CoA and acetyl-CoA producing/consuming reactions, it was determined that the
542 Uvaferm strain had the most significant disparity. This result aligns with the prediction of the
543 Uvaferm strain producing the most ethyl butanoate (Fig. 4). This detected mechanism for yeast to
544 produce MCFA ethyl esters to correct imbalances of CoA and acetyl-CoA has been hypothesized
545 before (Lambrechts and Pretorius, 2000). However, here we show that metabolic modeling
546 supports this view. Also, since MCFAs are toxic to yeast and, at sufficient concentrations, can lead
547 to stuck or sluggish fermentations (Viegas et al., 1989), strains better at producing ethyl esters
548 from CoA are predicted to achieve a fitness advantage.

549 Taken together, we report a model able to predict the main routes of ester formation over
550 the course of wine fermentation for different commercial yeast strains. Our results reveal that that
551 ester formation depends on intracellular acetyl-CoA/CoA levels. In addition, we gained novel
552 insights about metabolic routes taken to form key esters which pave the way for future metabolic
553 engineering strategies to manage ester content in alcoholic fermentations. For instance, one can
554 genetically modify an available GEM to delete, add, sub-express, or over-express, for a metabolite

555 of interest (Copeland et al., 2012). Then, appropriately calibrate the model using experimental
556 data, especially from sugar and nitrogenous substrates. Finally, one can examine the effect of
557 genetic modification and/or varying the substrate composition on the predictions of certain aroma
558 profiles.
559
560 **4 CONCLUSION**
561 As yeast becomes increasingly utilized by the food, biotechnology, and cosmetic sectors
562 to produce desirable aroma compounds organically, it is crucial to understand how the most
563 prominent of these alluring aromas are produced under industrially-related settings. By applying
564 an adapted dynamic flux balance analysis framework, this study was able to predict many aspects
565 of an experimental enological fermentation conducted using commercial wine strains, including
566 the production of primary metabolites and biomass, as well as key aromas, e.g., esters. By
567 observing from simulations that pivotal intracellular flux routes varied among the strains chiefly
568 during the carbohydrate accumulation phase, underlying mechanisms related to redox balance and
569 the utilization of acetyl-CoA were understood to be responsible for observed phenotypic behavior.
570 Moreover, the dynamic genome-scale modeling approach allowed the study of individual fatty
571 acid fluxes over time, supporting the potential role that certain ethyl esters form to remove toxic
572 fatty acids from the cell by previous experimental work. Future research should look further into
573 the genes regulating the acetyl-CoA, as mentioned above, with other commercial strains. This type
574 of research could establish a clearer, more general picture of how various types of aromas are
575 produced during yeast fermentation. Overall, the predictions agreed with previous experimental
576 findings and illustrated which metabolic pathways play a role in aroma production, making this a
577 promising approach for future use in studies related to individual fluxes of important metabolites

578 in oenological conditions and for comparing metabolic differences between commercial wine yeast
579 strains.

580

581 **ACKNOWLEDGEMENTS**

582 E. B-C. acknowledges funding from MCIU/AEI/FEDER, UE (grant reference: PID2021-
583 126380OB-C32), and Xunta de Galicia (IN607B 2020/03). In addition, some materials and
584 resources were funded by a Wageningen University and Research internal fund from the Food
585 Microbiology department.

586

587 ***Authors' contributions*: CRediT (Contribution Roles Taxonomy)-** Conceptualization, W.T.S.J.,
588 D.H, E.J.S., R.A.N., and E.B-C.; Data Curation, W.T.S.J. and D.H., Formal Analysis, W.T.S.J.,
589 D.H., and E.B-C.; Funding Acquisition, E.J.S. and E.B-C; Investigation, W.T.S.J.; Methodology,
590 W.T.S.J., D.H., and E.B-C.; Resources, R.A.N, and E.B-C.; Software, D.H, and E.B-C.;
591 Supervision, E.J.S, R.A.N., and E.B-C.; Validation, W.T.S.J.; Visualization, W.T.S.J., D.H., and
592 E.B-C; Writing—original draft, W.T.S.J.; Writing—review and editing, W.T.S.J., D.H., E.J.S.,
593 R.A.N., and E.B-C. All authors have read and agreed to the published version of the manuscript.

594

595 **CONFLICT OF INTEREST**

596 The authors declare no competing interests

597

598 **FIGURE CAPTIONS**

599 **Figure 1.** Details on the implementation of the multi-phase and multi-objective dynamic genome-
600 scale model to simulate batch fermentation. Multi-phase and multi-objective dynamic FBA and

601 methodology to compute dynamic flux rates. The process starts at t_0 ¼ 0 and ends at t_F; the timing
602 of each phase t_L, t_E, t_S, and t_D is computed through parameter estimation.

603 **Figure 2**. Overview of central carbon metabolism. Panels a to f depict model predictions versus
604 the experimental data on extracellular metabolite concentrations associated with glycolysis and
605 central carbon metabolism for the four strains. Panel g illustrates the predicted intracellular
606 dynamic flux ratios during the carbohydrate accumulation phase, showing how the four
607 commercial strains employ different redox balance strategies. These differences result in the
608 differential production of relevant external metabolites such as succinate (a), glycerol (d), ethanol
609 (e), and acetate (f).

610 **Figure 3**. Overview of higher-alcohol production. Panel a depicts the predicted intracellular flux
611 dynamic flux ratios related to higher alcohols: propanol, 2-phenylethanol (PEA), isobutanol, and
612 isoamylol during the carbohydrate accumulation phase and their related effect on the redox balance
613 of cofactors. Panels b to f represent a comparison between model predictions and experimental
614 values of PEA, threonine, propanol, isobutanol, and isoamylol, respectively.

615 **Figure 4**. Overview of acetate and fatty acid ethyl ester production. Panel a shows the predicted
616 intracellular dynamic flux ratios corresponding to the production of esters: 2-phenylethyl acetate,
617 isoamyl acetate, ethyl acetate, and ethyl butanoate during the carbohydrate accumulation phase
618 and their respective impact on the cofactor balance. Panels b to i correspond to the comparison
619 between model predictions and experimental data of 2-phenylethyl acetate, isoamyl acetate, ethyl
620 acetate, ethyl butanoate, respectively.

621 **Figure 5**. Comparative illustration of the fluxes through the reactions consuming and producing
622 acetyl-CoA during the carbohydrate accumulation phase, illustrating how acetyl-CoA/CoA ratios
623 modulate cellular phenotype.

624 **REFERENCES**.

625 Aung, H.W., Henry, S.A., and Walker, L.P. (2013) Revising the representation of fatty acid,
626 glycerolipid, and glycerophospholipid metabolism in the consensus model of yeast metabolism,
627 *Ind. Biotechnol.* **9**: 215-228.

628 Balsa-Canto, E., Alonso, A.A., and Banga, J.R. (2010) An iterative identification procedure for
629 dynamic modeling of biochemical networks, *BMC Syst. Biol.* **4**: 11.

630 Balsa-Canto, E., Henriques, D., Gábor, A., and Banga, J.R. (2016) AMIGO2, a toolbox for
631 dynamic modeling, optimization and control in systems biology, *Bioinformatics* **32**: 3357-3359.

632 Botstein, D., Chervitz, S.A., and Cherry, M. (1997) Yeast as a model organism, *Science* **277**: 1259-
633 1260.

634 Boulton, R. (1980) The prediction of fermentation behavior by a kinetic model, *Am. J. Enol. Vitic.*
635 **31**: 40.

636 Carrau, F.M., Medina, K., Farina, L., Boido, E., Henschke, P.A., and Dellacassa, E. (2008)
637 Production of fermentation aroma compounds by *Saccharomyces cerevisiae* wine yeasts: effects
638 of yeast assimilable nitrogen on two model strains, *FEMS Yeast Res.* **8**: 1196-1207.

639 Copeland, W.B., Bartley, B.A., Chandran, D., Galdzicki, M., Kim, K.H., Sleight, S.C., et al. (2012)
640 Computational tools for metabolic engineering, *Metabolic Engineering* **14**: 270-280.

641 Cramer, A.C., Vlassides, S., and Block, D.E. (2002) Kinetic model for nitrogen-limited wine
642 fermentations, *Biotechnol. Bioeng.* **77**: 49-60.

643 Dekoninck, T. (2012) Bottle conditioning of beer strategies to improve yeast refermentation
644 performance.

645 Dunn, B., Levine, R.P., and Sherlock, G. (2005) Microarray karyotyping of commercial wine yeast
646 strains reveals shared, as well as unique, genomic signatures, *BMC Genomics* **6**: 53.

647 Dzialo, M.C., Park, R., Steensels, J., Lievens, B., and Verstrepen, K.J. (2017) Physiology, ecology
648 and industrial applications of aroma formation in yeast, *FEMS Microbiol. Rev.* **41**: S95-S128.
649 Forster, J., Famili, I., Fu, P., Palsson, B.O., and Nielsen, J. (2003) Genome-scale reconstruction of
650 the *Saccharomyces cerevisiae* metabolic network, *Genome Research* **13**: 244-253.
651 François, J., and Parrou, J.L. (2001) Reserve carbohydrates metabolism in the yeast
652 Saccharomyces cerevisiae, *FEMS Microbiol. Rev.* **25**: 125-145.
653 Gonzalez, R., and Morales, P. (2017) Wine secondary aroma: understanding yeast production of
654 higher alcohols, *Microb. Biotechnol.* **10**: 1449-1450.
655 Heavner, B.D., Smallbone, K., Price, N.D., and Walker, L.P. (2013) Version 6 of the consensus
656 yeast metabolic network refines biochemical coverage and improves model performance,
657 *Database* **2013**.
658 Heirendt, L., Arreckx, S., Pfau, T., Mendoza, S.N., Richelle, A., Heinken, A., et al. (2019) Creation
659 and analysis of biochemical constraint-based models using the COBRA Toolbox v.3.0, *Nature*
660 *Protocols* **14**: 639-702.
661 Henderson, C.M., Lozada-Contreras, M., Jiranek, V., Longo, M.L., and Block, D.E. (2013)
662 Ethanol production and maximum cell growth are highly correlated with membrane lipid
663 composition during fermentation as determined by lipidomic analysis of 22 *Saccharomyces*
664 *cerevisiae* strains, *Appl. Environ. Microbiol.* **79**: 91-104.
665 Henriques, D., Balsa-Canto, E., and Druzhinina, I.S. (2021a) The Monod model is insufficient to
666 explain biomass growth in nitrogen-limited yeast fermentation, *Applied and Environmental*
667 *Microbiology* **87**: e01084-01021.
668 Henriques, D., Minebois, R., Mendoza, S.N., Macías, L.G., Pérez-Torrado, R., Barrio, E., et al.
669 (2021b) A multiphase multiobjective dynamic genome-scale model shows different redox

670 balancing among yeast species of the *Saccharomyces* genus in fermentation, *mSystems* **6**: e00260-
671 00221.
672 Herrgård, M.J., Swainston, N., Dobson, P., Dunn, W.B., Arga, K.Y., Arvas, M., et al. (2008) A
673 consensus yeast metabolic network reconstruction obtained from a community approach to
674 systems biology, *Nature Biotechnology* **26**: 1155-1160.
675 Hindmarsh, A.C., Brown, P.N., Grant, K.E., Lee, S.L., Serban, R., Shumaker, D.E., and
676 Woodward, C.S. (2005) SUNDIALS: Suite of nonlinear and differential/algebraic equation
677 solvers, *ACM Transactions on Mathematical Software (TOMS)* **31**: 363-396.
678 Hirst, M.B., and Richter, C.L. (2016) Review of aroma formation through metabolic pathways of
679 *Saccharomyces cerevisiae* in beverage fermentations, *Am. J. Enol. Vitic.* **67**: 361-370.
680 Hjersted, J.L., Henson, M.A., and Mahadevan, R. (2007) Genome-scale analysis of
681 Saccharomyces cerevisiae metabolism and ethanol production in fed-batch culture, *Biotechnol.*
682 *Bioeng.* **97**: 1190-1204.
683 Hong, K.-Q., Fu, X.-M., Dong, S.-S., Xiao, D.-g., and Dong, J. (2019) Modulating acetate ester
684 and higher alcohol production in *Saccharomyces cerevisiae* through the cofactor engineering, *J.*
685 *Ind. Microbiol. Biotechnol.* **46**: 1003-1011.
686 Ingledew, W., and Kunkee, R.E. (1985) Factors influencing sluggish fermentations of grape juice,
687 *Am. J. Enol. Vitic.* **36**: 65-76.
688 Jouhten, P., Wiebe, M., and Penttilä, M. (2012) Dynamic flux balance analysis of the metabolism
689 of Saccharomyces cerevisiae during the shift from fully respirative or respirofermentative
690 metabolic states to anaerobiosis, *The FEBS Journal* **279**: 3338-3354.
691 Lam, F.H., Ghaderi, A., Fink, G.R., and Stephanopoulos, G. (2014) Engineering alcohol tolerance
692 in yeast, *Science* **346**: 71-75.

693 Lambrechts, M., and Pretorius, I. (2000) Yeast and its importance to wine aroma-a review, *S. Afr.*
694 *J. Enol. Vitic* **21**: 97-129.
695 Lewis, N.E., Hixson, K.K., Conrad, T.M., Lerman, J.A., Charusanti, P., Polpitiya, A.D., et al.
696 (2010) Omic data from evolved *E. coli* are consistent with computed optimal growth from genome-
697 scale models, *Molecular Systems Biology* **6**: 390.
698 Liti, G. (2015) The fascinating and secret wild life of the budding yeast S. cerevisiae, *eLife* **4**:
699 e05835.
700 Lu, H., Li, F., Sanchez, B.J., Zhu, Z., Li, G., Domenzain, I., et al. (2019) A consensus *S. cerevisiae*
701 metabolic model Yeast8 and its ecosystem for comprehensively probing cellular metabolism,
702 *Nature Communications* **10**: 3586.
703 Machado, D., Rodrigues, L.R., and Rocha, I. (2014) A kinetic model for curcumin production in
704 *Escherichia coli*, *Biosystems* **125**: 16-21.
705 Mason, A.B., and Dufour, J.-P. (2000) Alcohol acetyltransferases and the significance of ester
706 synthesis in yeast, *Yeast* **16**: 1287-1298.
707 Miller, A.C., Wolff, S.R., Bisson, L.F., and Ebeler, S.E. (2007) Yeast strain and nitrogen
708 supplementation: Dynamics of volatile ester production in Chardonnay juice fermentations, *Am.*
709 *J. Enol. Vitic.* **58**: 470-483.
710 Minebois, R., Pérez-Torrado, R., and Querol, A. (2020) A time course metabolism comparison
711 among Saccharomyces cerevisiae, S. uvarum and S. kudriavzevii species in wine fermentation,
712 *Food Microbiol.* **90**: 103484.
713 Moreno-Paz, S., Schmitz, J., Martins dos Santos, V.A.P., and Suarez-Diez, M. (2022) Enzyme-
714 constrained models predict the dynamics of *Saccharomyces cerevisiae* growth in continuous, batch
715 and fed-batch bioreactors, *Microb. Biotechnol.* **n/a**.

716 Nookaew, I., Jewett, M.C., Meechai, A., Thammarongtham, C., Laoteng, K., Cheevadhanarak, S.,
717 et al. (2008) The genome-scale metabolic model iIN800 of *Saccharomyces cerevisiae* and its
718 validation: a scaffold to query lipid metabolism, *BMC Syst. Biol.* **2**: 71.
719 Orth, J.D., Thiele, I., and Palsson, B.O. (2010) What is flux balance analysis?, *Nature*
720 *Biotechnology* **28**: 245-248.
721 Pérez-Torrado, R., and Matallana, E. (2015) Enhanced fermentative capacity of yeasts engineered
722 in storage carbohydrate metabolism, *Biotechnol. Progr.* **31**: 20-24.
723 Pérez, D., Jaehde, I., Guillamón, J.M., Heras, J.M., and Querol, A. (2021) Screening of
724 *Saccharomyces* strains for the capacity to produce desirable fermentative compounds under the
725 influence of different nitrogen sources in synthetic wine fermentations, *Food Microbiol.* **97**:
726 103763.
727 Peter, J., De Chiara, M., Friedrich, A., Yue, J.X., Pflieger, D., Bergstrom, A., et al. (2018) Genome
728 evolution across 1,011 *Saccharomyces cerevisiae* isolates, *Nature* **556**: 339-344.
729 Pizarro, F., Varela, C., Martabit, C., Bruno, C., Prez-Correa, J.R., and Agosin, E. (2007) Coupling
730 kinetic expressions and metabolic networks for predicting wine fermentations, *Biotechnol. Bioeng.*
731 **98**: 986-998.
732 Qin, N., Li, L., Ji, X., Li, X., Zhang, Y., Larsson, C., et al. (2020) Rewiring Central Carbon
733 Metabolism Ensures Increased Provision of Acetyl-CoA and NADPH Required for 3-OH-
734 Propionic Acid Production, *ACS Synthetic Biology* **9**: 3236-3244.
735 Quiros, M., Martinez-Moreno, R., Albiol, J., Morales, P., Vazquez-Lima, F., Barreiro-Vazquez,
736 A., et al. (2013) Metabolic flux analysis during the exponential growth phase of *Saccharomyces*
737 *cerevisiae* in wine fermentations, *PLoS One* **8**: e71909.

738 Ribéreau-Gayon, P., Dubourdieu, D., Doneche, B., and Lonvaud, A. (2000) Biochemistry of
739 alcoholic fermentation and metabolic pathways of wine yeasts, *Handbook of Enology Volume* **1**:
740 51-74.
741 Rollero, S., Bloem, A., Camarasa, C., Sanchez, I., Ortiz-Julien, A., Sablayrolles, J.-M., et al.
742 (2015) Combined effects of nutrients and temperature on the production of fermentative aromas
743 by *Saccharomyces cerevisiae* during wine fermentation, *Appl. Microbiol. Biotechnol.* **99**: 2291-
744 2304.
745 Rossouw, D., Næs, T., and Bauer, F.F. (2008) Linking gene regulation and the exo-metabolome:
746 A comparative transcriptomics approach to identify genes that impact on the production of volatile
747 aroma compounds in yeast, *BMC Genomics* **9**: 530.
748 Saerens, S., Delvaux, F., Verstrepen, K., Van Dijck, P., Thevelein, J., and Delvaux, F. (2008)
749 Parameters affecting ethyl ester production by *Saccharomyces cerevisiae* during fermentation,
750 *Appl. Environ. Microbiol.* **74**: 454-461.
751 Saerens, S.M.G., Delvaux, F.R., Verstrepen, K.J., and Thevelein, J.M. (2010) Production and
752 biological function of volatile esters in *Saccharomyces cerevisiae*, *Microb. Biotechnol.* **3**: 165-
753 177.
754 Sainz, J., Pizarro, F., Pérez-Correa, J.R., and Agosin, E. (2003) Modeling of yeast metabolism and
755 process dynamics in batch fermentation, *Biotechnol. Bioeng.* **81**: 818-828.
756 Sánchez, B.J., Li, F., Kerkhoven, E.J., and Nielsen, J. (2019) SLIMEr: probing flexibility of lipid
757 metabolism in yeast with an improved constraint-based modeling framework, *BMC Syst. Biol.* **13**:
758 4.

759 Sánchez, B.J., Pérez-Correa, J.R., and Agosin, E. (2014) Construction of robust dynamic genome-
760 scale metabolic model structures of *Saccharomyces cerevisiae* through iterative re-
761 parameterization, *Metabolic Engineering* **25**: 159-173.
762 Sánchez, B.J., Zhang, C., Nilsson, A., Lahtvee, P.-J., Kerkhoven, E.J., and Nielsen, J. (2017)
763 Improving the phenotype predictions of a yeast genome-scale metabolic model by incorporating
764 enzymatic constraints, *Molecular Systems Biology* **13**: 935.
765 Schulze, U., Lidén, G., Nielsen, J., and Villadsen, J. (1996) Physiological effects of nitrogen
766 starvation in an anaerobic batch culture of Saccharomyces cerevisiae, *Microbiology* **142**: 2299-
767 2310.
768 Scott, W.T., Mastrigt, O.v., Block, D.E., Notebaart, R.A., Smid, E.J., and Cuomo, C.A. (2021a)
769 Nitrogenous Compound Utilization and Production of Volatile Organic Compounds among
770 Commercial Wine Yeasts Highlight Strain-Specific Metabolic Diversity, *Microbiology Spectrum*
771 **9**: e00485-00421.
772 Scott, W.T., Smid, E.J., Block, D.E., and Notebaart, R.A. (2021b) Metabolic flux sampling
773 predicts strain-dependent differences related to aroma production among commercial wine yeasts,
774 *Microb. Cell Fact.* **20**: 204.
775 Scott, W.T., Smid, E.J., Notebaart, R.A., and Block, D.E. (2020) Curation and analysis of a
776 *Saccharomyces cerevisiae* genome-scale metabolic model for predicting production of sensory
777 impact molecules under enological conditions, *Processes* **8**: 1195.
778 Seguinot, P., Rollero, S., Sanchez, I., Sablayrolles, J.-M., Ortiz-Julien, A., Camarasa, C., and
779 Mouret, J.-R. (2018) Impact of the timing and the nature of nitrogen additions on the production
780 kinetics of fermentative aromas by *Saccharomyces cerevisiae* during winemaking fermentation in
781 synthetic media, *Food Microbiol.* **76**: 29-39.

782 Snoek, T., Verstrepen, K.J., and Voordeckers, K. (2016) How do yeast cells become tolerant to
783 high ethanol concentrations?, *Curr. Genet.* **62**: 475-480.
784 Steensels, J., Meersman, E., Snoek, T., Saels, V., Verstrepen, K.J., and Cullen, D. (2014) Large-
785 scale selection and breeding To generate industrial yeasts with superior aroma production, *Applied*
786 *and Environmental Microbiology* **80**: 6965-6975.
787 Su, Y., Heras, J.M., Gamero, A., Querol, A., and Guillamón, J.M. (2021) Impact of nitrogen
788 addition on wine fermentation by *S. cerevisiae* strains with different nitrogen requirements, *J.*
789 *Agric. Food. Chem.* **69**: 6022-6031.
790 Taylor, G.T., and Kirsop, B.H. (1977) The origin of the medium-chain length fatty acids present
791 in beer, *J. Inst. Brew.* **83**: 241-243.
792 Tesnière, C., Brice, C., and Blondin, B. (2015) Responses of *Saccharomyces cerevisiae* to nitrogen
793 starvation in wine alcoholic fermentation, *Appl. Microbiol. Biotechnol.* **99**: 7025-7034.
794 Varela, C., Pizarro, F., and Agosin, E. (2004) Biomass content governs fermentation rate in
795 nitrogen-deficient wine musts, *Appl. Environ. Microbiol.* **70**: 3392-3400.
796 Vargas, F.A., Pizarro, F., Pérez-Correa, J.R., and Agosin, E. (2011) Expanding a dynamic flux
797 balance model of yeast fermentation to genome-scale, *BMC Syst. Biol.* **5**: 75.
798 Varma, A., and Palsson, B.O. (1994) Stoichiometric flux balance models quantitatively predict
799 growth and metabolic by-product secretion in wild-type *Escherichia coli W3110*, *Applied and*
800 *Environmental Microbiology* **60**: 3724-3731.
801 Viegas, C.A., Rosa, M.F., Sá-Correia, I., and Novais, J.M. (1989) Inhibition of yeast growth by
802 octanoic and decanoic acids produced during ethanolic fermentation, *Applied and Environmental*
803 *Microbiology* **55**: 21-28.

Walter, E., and Pronzato, L. (1997) *Identification of parametric models from experimental data*. Berlin; New York; Paris: Springer ; Masson.

Phases, objectives and dynamic flux ratios

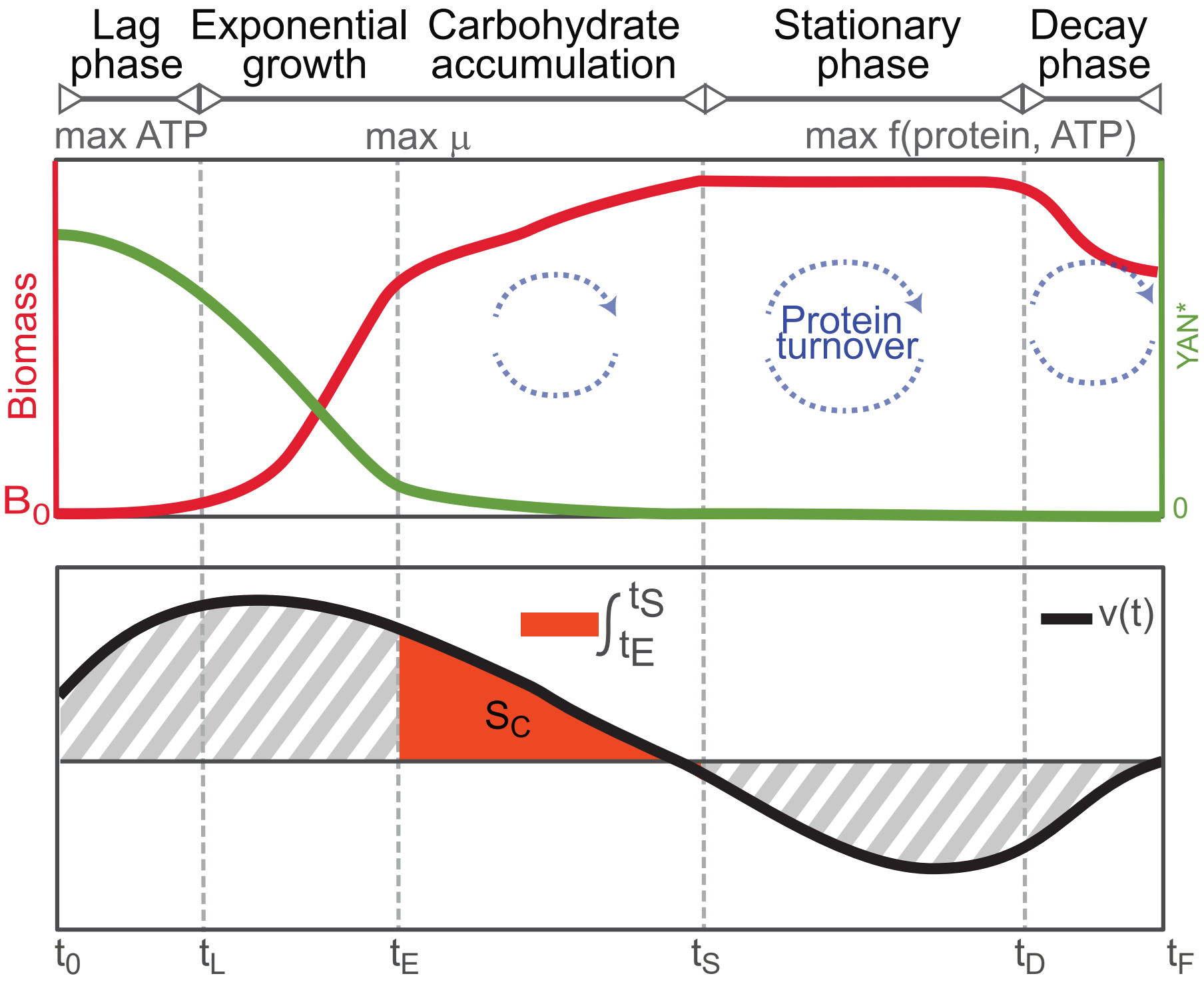

Predicted dynamic flux ratios

Central carbon metabolism

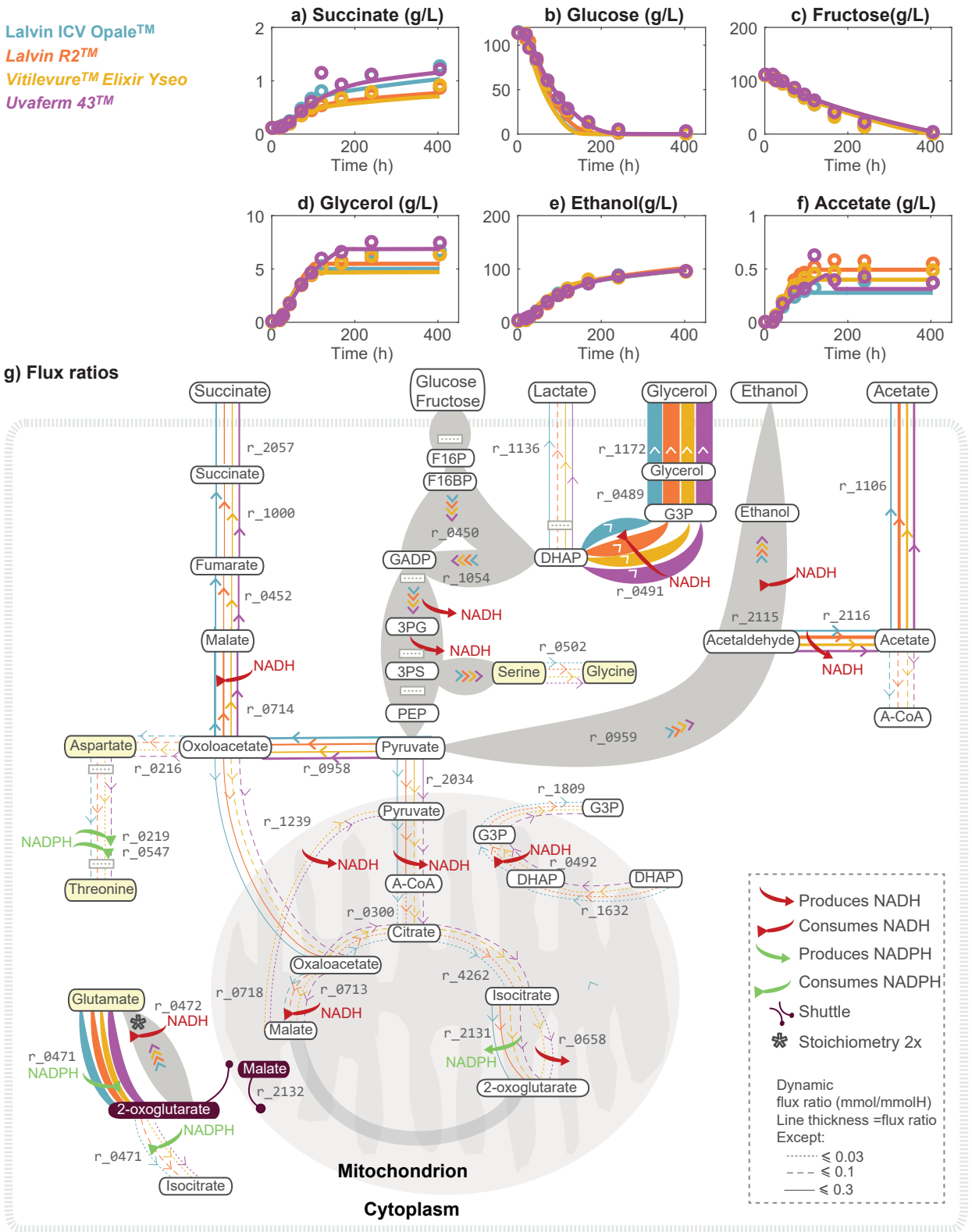

Production of higher alcohols

a) Flux ratios

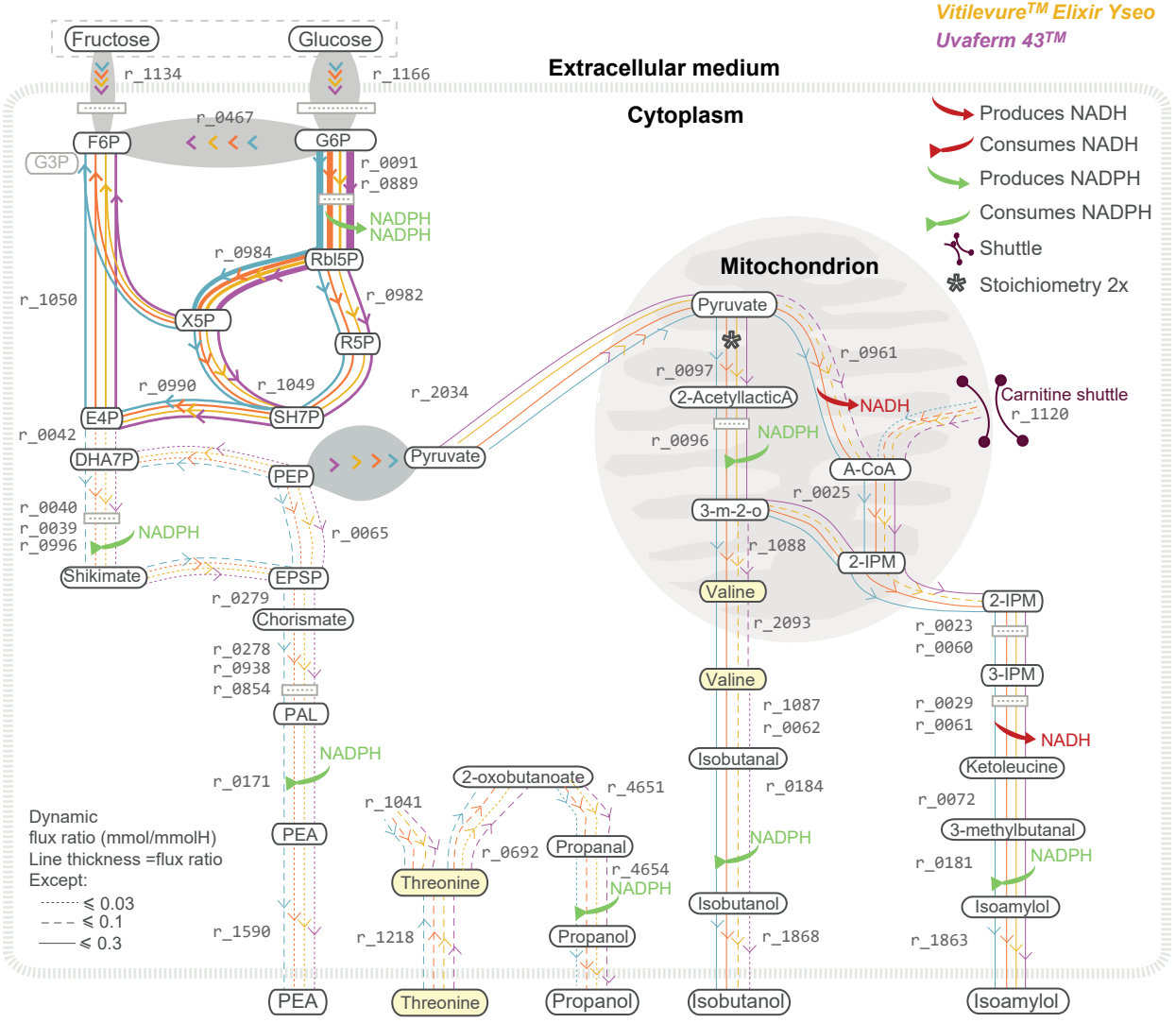

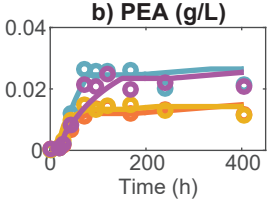

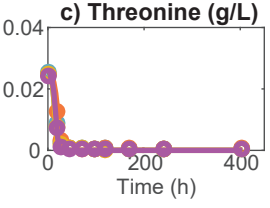

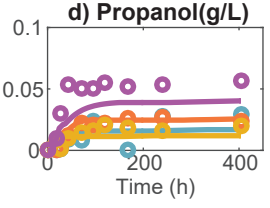

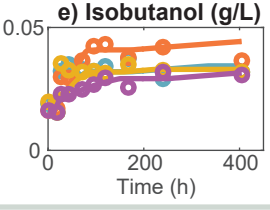

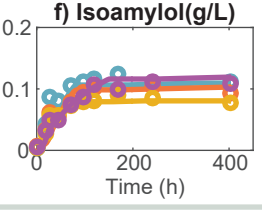

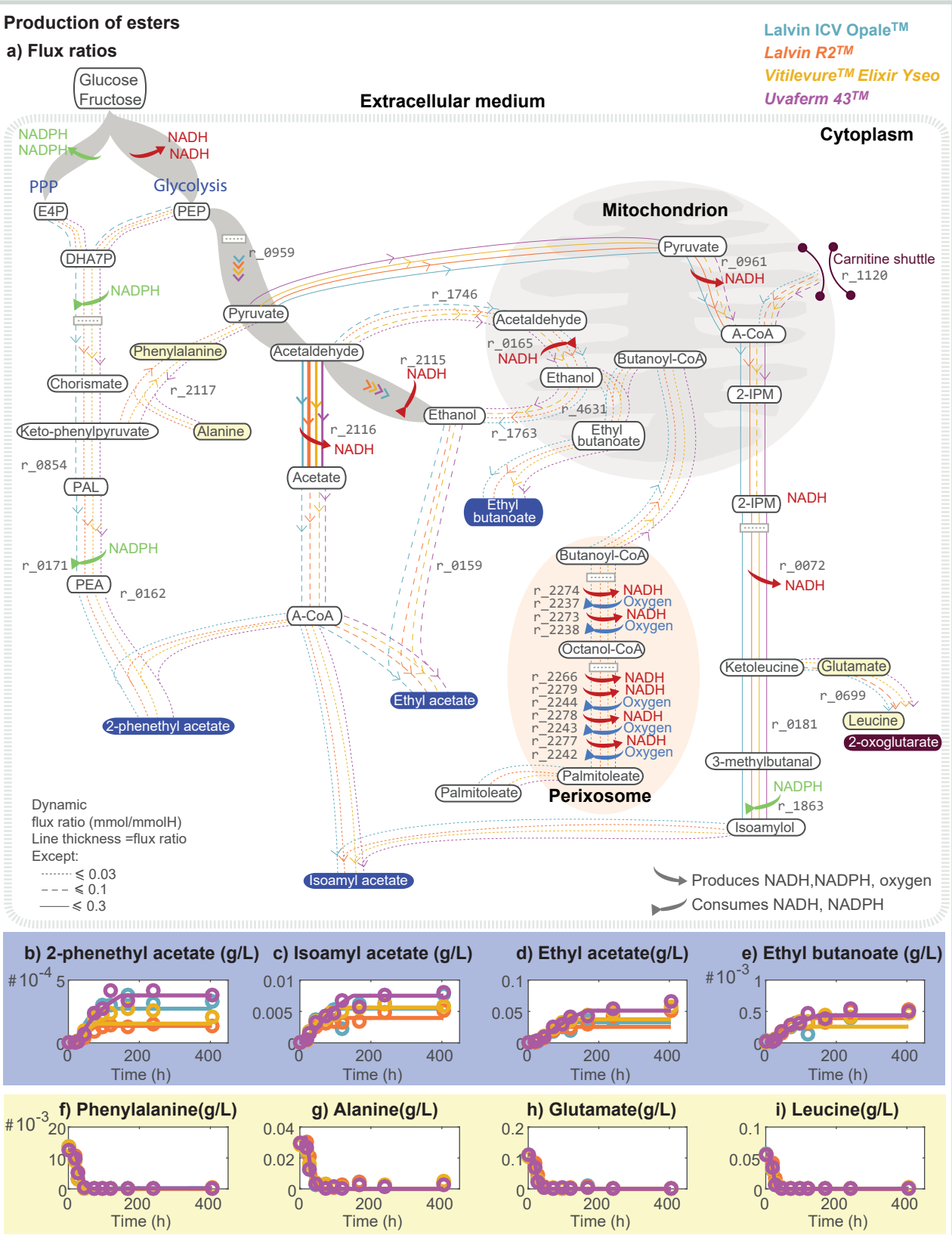
Production of esters
a) Flux ratios
Lalvin ICV Opale™
Lalvin R2™
Vitilevure™ Elixir Yseo
Uvaferm 43™
Extracellular medium
Cytoplasm
Mitochondrion
Perixosome
Glucose
Fructose
NADPH
NADPH
NADH
NADH
PPP
Glycolysis
E4P
PEP
DHA7P
r_0959
Pyruvate
Phenylalanine
Acetaldehyde
Chorismate
r_2117
Keto-phenylpyruvate
Alanine
r_0854
PAL
r_0171
PEA
r_0162
r_2115
r_2116
Acetate
A-CoA
r_1746
r_0165
Ethanol
r_4631
r_1763
Ethyl butanoate
r_0159
Ethyl acetate
2-phenethyl acetate
Isoamyl acetate
Butanoyl-CoA
r_2274
r_2237
r_2273
r_2238
Oxygen
Octanol-CoA
r_2266
r_2279
r_2244
r_2278
r_2243
r_2277
r_2242
Palmitoleate
Pyruvate
r_0961
Carnitine shuttle
r_1120
A-CoA
2-IPM
r_0072
Ketoleucine
Glutamate
r_0699
Leucine
2-oxoglutarate
r_0181
3-methylbutanal
r_1863
Isoamylol
Dynamic
flux ratio (mmol/mmolH)
Line thickness =flux ratio
Except:
≤ 0.03
≤ 0.1
≤ 0.3
Produces NADH,NADPH, oxygen
Consumes NADH, NADPH
b) 2-phenethyl acetate (g/L)
c) Isoamyl acetate (g/L)
d) Ethyl acetate(g/L)
e) Ethyl butanoate (g/L)
f) Phenylalanine(g/L)
g) Alanine(g/L)
h) Glutamate(g/L)
i) Leucine(g/L)
Time (h)
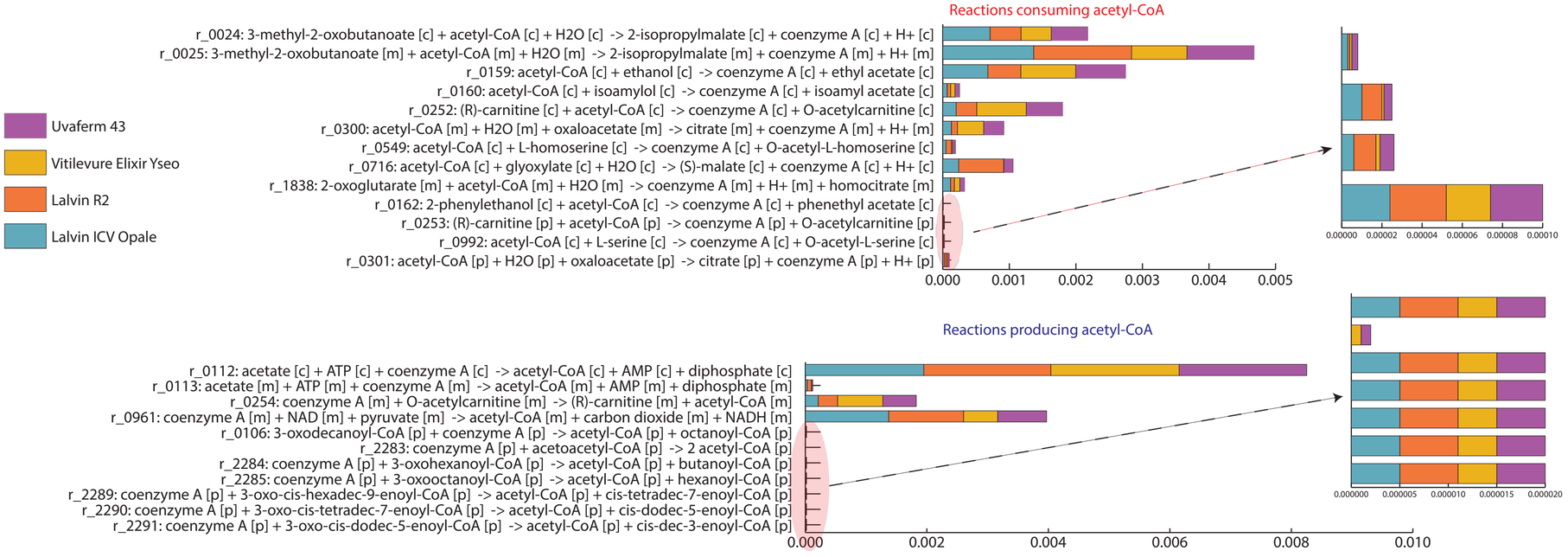
Dynamic flux ratios that contribute to cofactor (acetyl-CoA/CoA) balance